Title: A Red light Powered Silicon Nanowire Biophotochemical Diode for Simultaneous CO_2 Reduction and Glycerol Valorization

Author list: Jimin Kim[1,†], Jia-An Lin[2,†], Jinhyun Kim[2,3], Inwhan Roh[2], Soohyung Lee[2], Peidong Yang[1,2,4,5*]

Affiliations:

[1] Department of Materials Science and Engineering, University of California, Berkeley; Berkeley, CA, 94720, USA.

[2] Department of Chemistry, University of California, Berkeley; Berkeley, CA, 94720, USA.

[3] Department of Chemical and Biomolecular Engineering, University of California, Berkeley; Berkeley, CA, 94720, USA.

[4] Materials Sciences Division, Lawrence Berkeley National Laboratory; Berkeley, CA, 94720, USA.

[5] Kavli Energy Nanosciences Institute; Berkeley, CA, 94720, USA.

[†] These authors contributed equally to this work.

*To whom correspondence should be addressed: p_yang@berkeley.edu.

Abstract:

A bias-free photochemical diode, connecting a p-type photocathode and an n-type photoanode to harness light for driving photoelectrochemical reduction and oxidation pairs, serves as a platform for realizing light-driven fuel generation from CO_2. However, the conventional design, coupling cathodic CO_2 reduction with anodic oxygen evolution (OER), requires substantial energy input. Here, we present a photochemical diode device that harnesses red (740 nm) light to simultaneously drive biophotocathodic CO_2-to-multicarbon conversion and photoanodic glycerol oxidation as an alternative to OER to overcome the thermodynamic limitation. The device consists of an efficient CO_2-fixing microorganism, *Sporomusa ovata,* interfaced with a silicon nanowire (SiNW) photocathode and a Pt-Au loaded SiNW photoanode. This photochemical diode operated bias-free under low-intensity (20 mW/cm^2) red light irradiation with ~80% faradaic efficiency for both cathodic and anodic products. This work provides an alternative photosynthetic route to mitigate excessive CO_2 emissions and efficiently generate value-added chemicals from CO_2 and glycerol.

Main text:

Introduction

The intermittent nature of sunlight poses a challenge in powering our society on a practical scale[1,2]. An appropriate technology to store renewable energy for use when the sun is not shining is necessary. One possible solution is to utilize the photon energy to drive uphill chemical reactions to produce chemical fuels that can be stored and transported for later use. Photoelectrochemical (PEC) CO_2 reduction is a promising route to store light energy in chemical bonds and to promote carbon neutrality[3–6]. In a photochemical diode first proposed by Nozik, a p-type semiconductor photocathode and an n-type semiconductor photoanode are wired together to drive reduction and oxidation reactions with a p/n-PEC device configuration[7,8]. The photoexcited charge carriers within a solid-state semiconductor electrode are transferred to reactants, for instance, CO_2 molecules dissolved in a cathodic electrolyte, at the solid-liquid junction to drive redox reactions.

The working principle of such a device is that the total harvested light energy from both photoelectrodes should be larger than the thermodynamic energy requirement plus kinetic overpotentials for oxidation and reduction reactions [9]. While the photochemical diode approach has been showcased for a thermodynamically and kinetically more accessible hydrogen evolution reaction (HER), limited success has been achieved for a CO_2 reduction reaction (CO_2RR) due to the higher catalytic overpotentials of currently reported abiotic CO_2 catalysts [8,10–12]. For example, an Au-loaded amorphous Si photocathode combined with a bismuth vanadate photoanode was recently shown to enable a bias-free PEC system for CO_2RR. Still, the reduction products were CO, a simple 2-electron reduced product, and parasitic H_2 with a low operating photocurrent density (J_{op}) of 0.24 mA cm^{-2} [13]. Incorporating photovoltaic

components, such as embedded perovskite photovoltaics, into PEC systems helps to increase the total photovoltage and has been shown to produce C_2 and C_3[14,15] with Cu electrocatalysts, though it still operated at very limited bias-free J_{op}. It also complicates the device structure and increases the system costs. A bias-free PEC device to reduce CO_2 to more reduced products beyond CO has yet to be achieved for the abiotic version of the photochemical diode.

The challenge posed by the excessive overpotentials associated with inorganic catalysts can be effectively mitigated by utilizing CO_2-reducing biocatalysts that operate with minimal overpotentials near the standard thermodynamic potentials of given reactions. By capitalizing on an overpotential of less than 200 mV exhibited by the acetogenic bacterium *Sporomusa ovata* (*S. ovata)*[16,17], a $Si - TiO_2$ nanowire biophotochemical diode was employed to achieve bias-free CO_2-to-acetate synthesis with a J_{op} of ~0.3 mA/cm^2 and a solar-to-chemical efficiency of 0.38%[17]. This acetate, derived from CO_2, functioned as a readily available substrate for the synthesis of high-value chemicals, including n-butanol, polyhydroxybutyrate (PHB), and N_2 fixation, using various strains of microorganisms, such as *Escherichia coli*[17]*, C. Basilenisis*[18]*, and R. Pal*[19].

However, further enhancements in the bias-free photocurrent density of the system are necessary for its widespread application. Notably, two limiting factors contributing to the low J_{op} can be pointed out: the overly oxidative thermodynamic potential of OER ($E_{H2O/O2}$ = 1.23 V vs. RHE) and the sluggish CO_2-reducing kinetic rates, originating from the slow CO_2 turnover rates of wild-type *S. ovata.* These limitations are illustrated by the resulting low crosspoint (J_{op} under the bias-free condition) of two reactions in Fig. 1A. An expanded concept of the photochemical diode can encompass alternative oxidation reactions with faster kinetics

and lower overpotential requirements. For instance, glycerol oxidation exhibits standard thermodynamic potentials between 0.14 – 0.41 V vs. RHE, depending on the products[20], and it shows a low overpotential of 200 mV when suitable catalysts are employed[21]. Thus, this approach could induce a negative shift in the oxidation curve, improving the overlapping current density between the photocathode and photoanode, thereby reducing the overall photovoltage demand and enhancing J_{op}. To address the second challenge on the biocathodic side, enhancing the CO_2 turnover rates through metabolic engineering, such as adaptive laboratory evolution of biocatalysts, can be readily employed[22]. By increasing the turnover rate of *S. ovata*, an enhancement in J_{op} towards C_{2+} products and overall solar-to-chemical conversion efficiency can be achieved under bias-free operation. These two strategies lead to the high J_{op} of the two reactions in Fig. 1B.

With this proposed alternative concept of artificial photosynthesis, here, we developed a biophotochemical device combining a p-type SiNW photocathode integrated with *S. ovata* and a Pt-Au loaded n-type SiNW photoanode. The schematics of the device structure are shown in Fig. 1C and 1D. The nanofabricated silicon wafers served as efficient and inexpensive photoelectrodes (Fig. 1E). The electroactive bacterium, *S. ovata,* is directly interfaced with the SiNW photocathode to uptake photogenerated reducing equivalents, e.g., hydrogen molecules and electrons, and utilize them to reduce CO_2 into acetate by the Wood−Ljungdahl pathway (WLP). The whole-cell catalysts were operated at more positive potentials than the thermodynamic potential of CO_2-to-acetate reduction (0.123 V vs. RHE) with the aid of photovoltage generated by SiNW under red light irradiation. With the bacteria-SiNW photocathode, a Pt-Au loaded n-type SiNW photoanode was wired in parallel for glycerol oxidation reaction (GOR), producing economically valuable oxidation products from glycerol, which is a main byproduct of biodiesel production [23]. 0.85 V of photovoltage was generated by

the PEC device under a low-intensity (20 mW/cm^2) of 740 nm LED and was sufficient to simultaneously drive biological CO_2 reduction reaction (CO_2RR) and GOR (Fig. 1C). This silicon p/n configuration photochemical diode achieved a maximum J_{op} of ~1.2 mA/cm^2 — where we report an appreciable bias-free PEC CO_2-to-C_2 reducing photocurrent density—with high faradaic efficiency, ~80% from both cathodic and anodic reactions.

Results

Fundamentals of photoelectrochemistry of SiNW in neutral pH

The PEC performance of the photocathode was first abiotically investigated under red light irradiation and biocompatible operating conditions of neutral pH in brackish bacterial medium for efficient hydrogen evolution (Fig. 2A - D). The hydrogen produced from the photocathode, which is a key reducing equivalent of WLP[24], attracts a floating *S. ovata* in the electrolyte to the electrode surface, facilitates their growth on the electrode, and leads to forming a robust bacteria-nanowire hybrid for CO_2 conversion. The wavelength of the red light used here, 740 nm, is well below that of the bandgap of silicon, 1100 nm, to efficiently excite the charge carriers while minimizing the thermalization loss and avoiding the antimicrobial activity associated with high-energy photons[25–28]. For the fabrication of a stable high-photovoltage SiNW photocathode, an n^+ shell was formed on a p-type SiNW array to increase the photovoltage, and 30 nm of crystalline titanium dioxide (TiO_2) was deposited by atomic layer deposition (ALD) to protect the substrate from corrosion (Supplementary Fig. 1)[29–32]. Then, a 3 nm Pt was sputtered on the top surface as a co-catalyst to facilitate the charge transfer to the electrolyte. Nickel was also tested as a co-catalyst due to its good biocompatibility[33,34] and facile connection to membrane-bound proteins[35]. However, the photocathodes with sputtered Pt exhibited noticeably higher PEC performances, 200 mV more positive onset potential and four times higher photocurrent density, 1.4 mA/cm^2 and 0.36 mA/cm^2 at 0.1 V vs. RHE (Supplementary Fig. 2). Thus, Pt was used as a co-catalyst for the following experiments.

The fabricated Pt/TiO_2/n^+p-SiNW photocathode shows an onset potential of ~0.4 V vs. RHE under 20 mW/cm^2 red light irradiation (Fig. 2A). The dark and chopped scan corroborates that the photocurrents were generated under light irradiation. The control experiments revealed that the n^+ radial shell adds 200 mV of photovoltage, and the device exhibits a total photovoltage of ~400 mV under irradiation relative to dark Pt electrodes (Supplementary Fig. 3A and 3B). The influence of light intensity ranging from 20 mW/cm^2 to 7 mW/cm^2 on the photocurrents is shown in Fig. 2b. The lower light intensity yielded decreased photocurrent and photovoltage, as previously reported for the similar array-type Si photocathode[31]. The light intensity of 20 mW/cm^2 was selected for the following experiments because this intensity matches the daily average intensity of the infrared A (IR-A) radiation (760 nm – 1400 nm) of the solar spectrum so that the condition could closely simulate ambient irradiation conditions[36]. The intensity also offers the onset voltage of ~0.4 V vs. RHE, which sufficiently overlaps with the onset of GOR Si photoanode, ~0 V vs. RHE, for later integration into a combined system[21].

The effect of electrolyte bulk pH was also investigated (Fig. 2C). Su *et al.* previously demonstrated that lowering an initial bulk pH from 7.2 to 6.4 facilitates the formation of a close-packed bacteria-nanowire cathode[37]. The bulk pH of 7.2 could create a local microenvironment around SiNW with a highly basic pH exceeding 9, which is an inhospitable pH for the microorganism[37]. Thus, 50 mM of a zwitterionic MES (2-(N-morpholino)ethanesulfonic acid) buffer was added to the bacterial medium to enhance buffering capacity in the lower pH range (see methods for detailed composition). This buffering agent has a pK_a of 6.27, providing enhanced buffering capacity at the pH near its pKa compared to the conventional phosphate buffer, which has a pK_a of 7.21[38]. The presence of the buffer had no discernible effect on the metabolism of *S. ovata,* as demonstrated by comparing their growth

in cultures with and without MES buffer (Supplementary Fig. 4). Fig. 2C clearly shows pH dependency of the photocurrent from 6.2 to 7.2. This is presumably because the catalytic rate of HER on Pt and the resulting consumption of proton is high relative to the supply of protons from the local environment in the neutral pH. Consequently, a lower bulk pH, creating a lower local pH and facilitating faster proton supply, increases the overall reaction rate. To establish a hospitable microenvironment and provide a faster flux of reducing equivalents to the microorganisms, pH 6.2 of the MES-containing bacterial medium was used for subsequent experiments. Since a pH lower than 6.0 could decrease the buffering capacity of MES buffer and the optimal pH for *S. ovata* is 6.3[39], the pH was not further lowered. Fig. 2D shows a stable photocurrent of the abiotic photocathode in the MES buffer for over 12 hours at 0.15 V vs. RHE, which is close to the expected working potential of the bioCO_2RR-GOR bias-free system. The bulk pH increased slightly after the PEC operations of ~12 hours due to proton consumption from HER but was well mitigated at around 6.57 ± 0.13 (n = 3). Additionally, there was no production of acetates observed at these abiotic PEC conditions due to the excellent HER activity of platinum, despite continuous CO_2 gas feeding into the PEC device (Supplementary Fig. 5).

Lastly, Fig. 2E shows the linear sweep voltammetry (LSV) scans of a standard 0.5 M sulfuric acid and the biocompatible buffer electrolyte without iR-correction. Biocompatible buffers typically have an ionic concentration below 0.1 M to avoid osmotic stress which can diminish the productivity of bacteria[40]. Consequently, the bacterial medium used in this study exhibited a relatively higher ohmic drop than standard sulfuric acid due to its higher solution resistance, as shown in the electrochemical impedance spectroscopy (EIS) results in the inset of Fig. 2E. Although an additional electrolyte engineering for biocatalysts might reduce the ohmic drop and enhance the electrochemical performances as suggested by the microbial electrosynthesis

179 research community[41,42], the voltage drop remained modest around the expected operating
180 current density of the bias-free system, e.g., ~0.2 V of drop at 1 mA/cm^2.

181

182 **PEC half-reactions of biological CO_2RR and GOR**

183 Next, the microbial catalysts were incorporated onto this abiotic photocathode to form a
184 nanowire-bacteria hybrid and upgrade the chemistry from HER to CO_2RR. Two strains of *S.*
185 *ovata* were tested under the photocathodic condition: wild-type and a methanol-adapted strain.
186 Tremblay et al. reported that the methanol adaptation yields strain met-T18-2 with a faster
187 autotrophic metabolism[43], and the strain was successfully hybridized with a silicon nanowire
188 cathode by Kim et al[22]. From chronoamperometry experiments over 60 hours, the adapted
189 strain exhibited a ~5-fold increase in photocurrent density compared to the initial and that of
190 the wild-type strain (Fig. 3A). Fig. 3B and 3C show scanning electron microscopy (SEM)
191 images of the nanowire-bacteria hybrid after the PEC operations for the two strains. This
192 enhanced performance of adapted *S. ovata* over wild-type *S. ovata* is attributed to its faster
193 ability to uptake electrons and hydrogen[22]. Even though both strains started from the same
194 bacterial loading density (OD_{545} ~0.04 in the electrolyte), the adapted strain's faster
195 metabolism resulted in quicker reproduction, as clearly shown in the two SEM images after 60
196 hours of operation. The more direct attachment of biocatalysts creates more charge transfer
197 channels at the abio-bio interface and increases the photocurrent density at the same
198 potential[37,44]. Also, it must be noted that the increased biocatalyst loading on the photocathode,
199 which fully covered the surface of the photocathode, did not negatively affect the photocurrent
200 generation; instead, it increased it. This shows that the rate of PEC CO_2 reaction is limited by
201 the biocatalysts and stresses the importance of introducing efficient catalysts at the interface.
202 With superior metabolic activity on photocathodes, adapted *S. ovata* was used for the following
203 experiments. Fig. 3D shows the LSV of the biotic and abiotic photocathodes. Both exhibit a

similar cathodic onset potential of ~0.4 V vs. RHE, and the biophotocathode shows a slightly higher kinetic rate. This can be attributed to the simultaneous consumption of reaction products by microorganisms, which can enhance the reaction rate. Also, the acetates produced from CO_2 reduction and present in the electrolyte could enhance the overall buffering capacity of the electrolyte. The LSV scans of the biophotocathode under dark and chopped irradiation in Fig. 3E confirm a photo-induced electron transfer. The biophotocathodes with close-packed adapted *S. ovata* exhibit over 80% (n=3) of faradaic efficiency toward acetate (Supplementary Figs. 5, 6, and Supplementary Table 1). In addition, we confirmed no change in elemental components of the photocathode for the biotic and abiotic conditions after photoelectrolysis using low-energy energy-dispersive X-ray (EDX) analysis (Supplementary Fig. 7).

As a counter anodic reaction to CO_2RR, GOR was investigated on an n-type SiNW photoanode. GOR has recently gained attention as an efficient photoanodic reaction for PEC devices[45,46]. It has been reported that Pt-Au is a suitable GOR catalyst because it combines the advantages of the low overpotential of Pt and the high steady state current of Au synergistically[24]. Photoelectrochemically, co-sputtering Pt and Au on n-type planar Si could yield a very low onset potential of -0.05 V vs. RHE[21]. Also, GOR enables the production of high-value oxidation compounds, such as glyceric acid (GLA), providing an economic benefit[47]. We adopted a nanowire array structure, replacing the planar Si, and a p^+ shell was formed on a fabricated n-type SiNW and protected by 10 nm of ALD TiO_2. Then, we optimized the loading amount of the Pt-Au catalyst, considering the high surface area of the SiNW array (Supplementary Fig. 8). Fig. 3F shows the LSV scans of Pt-Au/TiO_2/p^+n-SiNW photoanode for GOR in 1 M KOH and 0.1 M glycerol under red light irradiation. Notably, the photoanode shows a ~0.45 V photovoltage shift relative to a dark Pt-Au on a glassy carbon electrode (Supplementary Fig. 9). Furthermore, the high-surface-area photoelectrode enhanced the

229 photocurrent near the onset potential (around 0 V vs. RHE) and offered a better fill factor
230 compared to the planar counterpart (Supplementary Fig. 9). This enhancement could be
231 attributed to the increased loading of Pt-Au catalysts, which improves the photocurrent density
232 in the lower potential region (around 0 V to 0.3 V vs. RHE) where the catalyst amount limits
233 the overall performance. Fig. 3G shows the overlap of the LSV scans between the photocathode
234 and photoanode, revealing an expected bias-free photocurrent density of ~ 1.2 mA/cm^2.

235

236 **Bias-free operation of SiNW photochemical diodes**

237 For the bias-free PEC setup, the photocathode and photoanode were placed into a two-chamber
238 cell separated by a bipolar membrane (BPM) (Fig. 1D). A utilization of BPM allows to separate
239 two different electrolytes with a significant pH difference[48]. This separation is crucial because
240 GOR is optimal in an alkaline environment with 1 M KOH, whereas microbial CO_2RR operates
241 at a neutral pH of 6.2 in the bacterial medium. The LSV scan of a two-electrode configuration
242 of photocathode and photoanode confirms the bias-free photocurrent density near 1.20 mA/cm^2
243 and the onset potential of -0.8 V (Fig. 4A). The long-term operation and the product analysis
244 of bias-free bioCO_2RR-GOR system are shown in Fig 4B and 4C. The integrated system was
245 able to maintain a photocurrent density of 1.2 mA/cm^2 after 1 hour. The main cathodic product
246 is acetate with a faradaic efficiency (FE) of 86.8 ± 14.0 %. The main anodic product is GLA,
247 with an FE of 38.8 ± 8.0%, and the total anodic product reaches an FE of 79.3 ± 9.1%. The rest
248 likely comes from products that are not analyzable through 1H NMR, such as tartronic acid
249 and carbonate. The production of glyceraldehyde and dihydroxyacetone was not detected
250 because both of them rearranged into lactic acid (LA) in alkaline conditions, making it hard to
251 differentiate them from the production of LA. The product distribution is similar to previously
252 reported PEC GOR results using the Pt-Au catalyst under similar conditions[21]. The acetate
253 production rate of the system was 44.8 ± 11.6 g/m^2·day and 0.1 g/L·day, which aligns with

values reported in microbial electrosynthesis (Supplementary Table 2). The bias-free photocurrent density of Pt-Au planar Si photoanode and SiNW biophotocathode was 0.12 ± 0.06 mA/cm^2, 7.2 times lower than that of SiNW photoanodes and SiNW biophotocathode, which highlights the effectiveness of such nanostructures in the PEC operation (Supplementary Fig. 10). Control experiments under dark indicate almost no photocurrent, less than 0.014 mA/cm^2, and consequently, negligible product formation, indicating that the products were mainly produced from photosynthesis (Supplementary Fig. 11). The pH changes of the cathodic chamber were analyzed from 6.17 ± 0.03 to 6.75 ± 0.05. The higher light intensity, e.g., 40 mW/cm^2 of irradiation, helped to increase the overall operating bias-free photocurrent to 1.6 mA/cm^2 (Supplementary Fig. 12). However, Su et al. found experimentally and computationally that the higher cathodic current (e.g., 1.5 mA/cm^2) kinetically forms a basic pH both in the bulk electrolyte and around the SiNW microenvironment (pH 8.4 and ≥pH 9.3, respectively)[37]. Similarly, the bulk catholyte was increased to ~8.0 after an 8-hour reaction. To further improve the production rate of the system, this local microenvironment issue could potentially be circumvented by adopting a flow system design or electrolyte engineering (see Supplementary Discussion 1 for more details).

Discussion

The bias-free photochemical device simultaneously driving biological CO_2 reduction and glycerol valorization under low-intensity red light was developed. The key to making this device work is using nature's efficient metabolic pathway for CO_2-to-C_2 reduction and replacing oxygen evolution with glycerol oxidation. The artificial photosynthetic reaction follows the overall formula with glyceric acid as an oxygenate product below:

$$2CO_2 + 2\ HOCH_2CH(OH)CH_2OH + h\nu \rightarrow CH_3COOH + 2HOCH_2CH(OH)COOH \quad (1)$$

It is noteworthy that this extended interpretation of biophotochemical diodes, replacing OER with GOR half-reaction, resembles the fundamental energy conversion principles exhibited by microorganisms. They can harness chemical energy by oxidizing inorganic sources (chemoautotrophs) and organic sources (heterotrophs), using these sources as electron donors. It not only facilitates the efficient conversion of CO_2 into C_{2+} products at high operating current densities but also enables the simultaneous transformation of organics into value-added chemicals, all under bias-free irradiated conditions. Supplementary Discussion 2 outlines the outlook of biophotochemical diodes.

The meticulously nanofabricated SiNW photoelectrodes can harvest 0.85 V from low-intensity red light irradiation. The integrated bias-free device coupling CO_2RR and GOR achieves a maximum of 1.2 mA/cm^2 of photocurrent density with over 80% faradaic efficiencies of C_2 product. The system achieved a high photocurrent density for PEC CO_2-to-C_2 reduction even under low light irradiance (Supplementary Table 3). Altogether, the photochemical diode device presented here provides a promising platform to utilize light energy to simultaneously convert CO_2 into valuable chemical bonds and upgrade glycerol through the synergistic combination of the efficient CO_2-fixing microorganism and the nanomaterials built from earth-abundant and inexpensive silicon.

Methods

Fabrication of p-SiNW and n-SiNW substrates

P-type boron-doped 6" Si wafers (Addison Semiconductor Materials, <100> oriented, 1-30 Ohm-cm, prime, double sided-polished) and n-type phosphorus-doped 6" Si wafers (Addison Semiconductor Materials, <100> oriented, 1-10 Ohm-cm, prime, single sided-polished) were used for the fabrication of SiNW array. The wafers were etched in a 4.9% HF bath for 3 minutes, thoroughly washed with DI water, and dried before fabrication processes. Afterward, hexamethyldisilazane was applied on the wafer for 2 minutes, and MiR 701 photoresist was spin-coated to have a thickness of 1 μm. 5x i-line photolithography stepper (GCA 8500) with a mask that is patterned with a square lattice of 3.75 μm circles and 10 μm pitches was used to pattern the wafer with a final photoresist pattern of 0.75 μm circles and 2 μm pitches. The wafer with the patterned photoresist was then developed using MF-26A for 60 seconds, descummed with oxygen plasma at 50 W for 60 seconds, and hard baked at 140 °C using UV light. A low-frequency inductive-coupled plasma deep reaction-ion etch (DRIE) process was employed (Surface Technology Systems Advanced Silicon Etch) to etch the wafer with O_2 and SF_6 as an etch gas and C_4F_8 as a passivation gas and a typical DRIE smooth-wall recipe was used. The etching process was stopped upon nanowire lengths of 21 μm were achieved. Afterward, any remaining photoresist was removed with O_2 plasma at 250 W for 7.5 minutes. For details on the nanowire fabrication, see ref. [29,30,49]

Fabrication of n^+p-SiNW and p^+n-SiNW substrates

A 6" Si wafer was used as a dopant carrier wafer for the doping of the fabricated p-SiNW or n-SiNW substrates. All the wafers were etched in a 4.9% HF bath for 3 minutes to remove native silicon oxides and were thoroughly washed with DI water and dried. The carrier wafer was spin-coated with either an arsenic silicate spin-on-dopant solution (Filmtronics, for n^+p-

SiNW fabrication) or a gallium silicate spin-on-dopant solution (Filmtronics, for p^+n-SiNW fabrication) at 2200 rpm for 30 seconds and baked on a hotplate at 150 °C for 30 minutes. Afterward, p-SiNW or n-SiNW array substrates, cleaned with HF, water, and acetone just before this process, were placed onto the carrier wafer upside down such that the nanowire surface is interfaced with the dopant layer. The two were placed into a rapid thermal annealing (RTA) chamber at 900 °C for either 180 seconds (for n^+p-SiNW fabrication) or 100 seconds (for p^+n-SiNW fabrication) under N_2. A spin-on-dopant thin film containing a high concentration of arsenic (for n^+ doping) or gallium (for p^+ doping) in SiO_2 networks was proximately contacted with SiNW substrates at a high temperature of 900 °C for the diffusion of the dopants. The photovoltage increase was tested on a planar substrate first to exclude the complexity of coherent doping on the nanostructured surfaces of SiNW, and the doping shell gave ~200 mV additional photovoltage for n^+p photocathode (Supplementary Fig. 3A). The silicon substrate surface should be free of native oxides and vapor molecules to prevent dopant rejections in SiO_2, where the dopants' solubility is much lower than that in silicon. A junction depth, x_j, where the concentrations of shell dopant and substrate dopant, e.g., arsenic and boron for n^+/p-Si, are equal, can be calculated based on the theoretical Gaussian distribution of dopants:

$$X_j = 2\sqrt{Dt}\, erfc^{-1}\left(\frac{N_B}{N_0}\right) \qquad (2)$$

where D is a diffusivity of dopant, and t is a diffusion time, N_B is a background concentration, and N_0 is a dopant concentration at the surface. N_0 can be extracted from a theoretical solubility of dopant in silicon at the temperature set for the RTA process. For instance, N_0 of arsenic, an n-type dopant, is 2×10^{20} at 900 °C, and x_j for the n^+ layer on p-Si is ~7 nm for 3 minutes at 900 °C of the RTA process.

TiO_2 protection layer deposition

The n^+p-SiNW and p^+n-SiNW substrates were cleaned in a 4.9% HF bath for 3 minutes, thoroughly washed with DI water and acetone, and then dried. Afterward, a 30 nm TiO_2 layer was deposited at 250 °C using atomic layer deposition (ALD) and titanium isopropoxide as the precursor (Picosun Atomic Layer Deposition system) for n^+p-SiNW, and a 10 nm ALD TiO_2 thin film was deposited at the deposition temperature of 200 °C and tetrakis(dimethylamido)titanium (TDMAT) as a precursor (Cambridge Fiji 200 Plasma ALD system) for p^+n-SiNW in order to maintain a stable device performance for extended operation time. It has been reported that this thin TiO_2 film on Si does not impede the charge transfer from Si to electrolyte and improves the stability of photoelectrodes[50,51]. Supplementary Fig. 13 shows the PEC performance of photoelectrodes with and without ALD TiO_2. After cooling, these substrates were stored in ambient air until use.

Deposition of Pt-Au and Pt catalyst

Pt-Au and Pt catalyst were deposited on the fabricated TiO_2/SiNW photoanode on a multi-target co-sputtering system (built in-house) with 3x3" sputter guns (TORUS Mag Keeper) supplied by two 2 kW pulsed DC power supplies and a 1.5 kW DC power supply, as previously reported[21]. After the deposition of the TiO_2 protection layer, around 3 nm of Pt catalyst was sputtered onto n^+p-SiNW substrates with 30 seconds of 50 W power applied on a Pt target. Pt-Au catalyst with a thickness of ~11 nm was co-sputtered onto p^+n-SiNW substrates with 45 seconds of 50 W power on a Pt target and 28 W power on a Au target[21]. Both Pt/n^+p-SiNW and Pt-Au/p^+n-SiNW substrates were stored in ambient air until use.

Electrode Preparation

For the photoelectrochemical (PEC) experiments, the nanofabricated Pt/TiO_2/n^+p-SiNW and Pt-Au/TiO_2/p^+n-SiNW substrates were utilized as photoanode and photocathode, respectively, and electrically conductive contacts to a titanium foil were formed. To do this, a Ga-In eutectic

was applied and then scratched on the back of the Si substrate. Later on, a quick-drying silver paste was applied on the top of the scratched Si substrate and fixed on the titanium foil using double-sided conductive carbon tapes as previously reported[17,22]. The electrodes were left to dry for 30 minutes in ambient conditions before being assembled on the cell for PEC chracterization.

PEC characterization

All experiments were performed within a set of custom-built PEC cells. The setup is a two-chamber PEC cell, a cathodic chamber with a working electrode and a reference electrode (CH instruments, Ag/AgCl, 1M KCl) and a Pt wire counter electrode in an anodic chamber. The working electrode is sealed with an X-ring with a contact area of 0.321 cm^2. A gas inlet and an outlet are embedded to flow CO_2-containing gas for the photocathodic experiments. The two chambers were separated by a bipolar membrane. Each chamber contains a quartz window for PEC experiments. A 740 nm uniform irradiation LED (Mightex Systems) with a power of 20 mW/cm^2 was used for the PEC experiments and calibrated with a certified silicon photodiode. The absorbance spectra of SiNW photocathode, photoanode, and bacteria are shown in Supplementary Fig. 14. The chopped scan group in linear sweep voltammetry was conducted by periodically blocking the optical path of light with a metal plate. During biophotocathodic experiments, the setup was left at the optimal growth temperature of *S. ovata,* which fluctuated between 28 and 30 °C. All the PEC experiments were performed with Gamry Interface 1000/600 potentiostats (Gamry Instrument). FE and J were both characterized vs. RHE defined as follows:

$$\text{V vs. RHE (V)} = \text{V vs. Ag/AgCl} + 0.237 + 0.059*\text{pH} \qquad (3)$$

The pH of a used electrolyte for an extended operation was often remeasured to get a precise value. For the bias-free operation, the silicon photocathode and photoanode were assembled in the same two-chamber PEC cell with the X-rings. The photocathode was used as a working electrode, the photoanode was used as a counter electrode, and the voltage of the working electrode was set to 0 V versus the counter electrode.

Bacterial strains and growth protocols

Wild-type *S. ovata* (DSM 2662), purchased from the American Type Culture Collection (ATCC), and the methanol-adapted *S. ovata* strain, prepared as detailed in ref.[22] and stored in a -80 °C freezer, were used in the experiments. The strains were stored as aliquots with 10% DMSO as a cryoprotectant. ATCC 1425 medium (resazurin omitted; yeast extract added) was used as a standard bacterial growth medium. Anaerobically prepared media, boiled under N_2 gas, was stored under =80% N_2/20% CO_2 in anaerobic hungate culture tubes (CLS-4208, Chemglass) with flange style butyl rubber stoppers and screw thread caps for heterotrophic cultures, or 18 × 150 mm Balch-type anaerobic culture tubes (CLS-4209, Chemglass) with chlorobutyl rubber stoppers and crimped aluminum seals for autotrophic cultures. To prepare a bacterial cell for experiments, the frozen cells were first revived in betaine medium (Supplementary Table 4) and cultured for two cycles in the betaine medium. *S. ovata* was incubated at 34 °C with a starting pH of 7, measured by a pH strip. The growth of *S. ovata* was monitored by measuring optical absorbance at 545 nm by a Spectrovis Plus Spectrophotometer (Venier). The growth of *S. ovata* typically reaches ~0.4 OD_{545} within two days of cultures in the betaine medium.

Formation of *S. ovata*-nanowire hybrids

The preparation of nanowire-bacteria hybrids were slightly modified from the previous reports using dark electrochemical conditions[22,37]. The nanowire-bacteria hybrids were prepared on

419 the SiNW photocathodes with the inorganic medium with 50 mM of MES as an electrolyte and
420 740 nm irradiation as a photon source. The pH value of the electrolyte was adjusted if needed
421 by adding a corresponding amount of hydrochloric acid or 1M sodium hydroxide into buffer
422 and a digital pH meter (Mettler Toledo) was used to measure the pH by taking out 5 ml of pH-
423 adjusted buffer after 30-minute of equilibration time. The pH-adjusted electrolyte were added
424 to the the acid sterilized cathodic (15 ml) and anodic (30ml) chambers, respectively. Abiotic
425 chronoamperometry experiments were conducted typically at ~0.3 V vs. RHE for a day with
426 purging 80% N_2/10% H_2/10% CO_2 gas to make anaerobic environment. In parallel, the revived
427 cells in the betaine medium were autotrophically cultured twice in yeast medium
428 (Supplementary Table 4) with 80% H_2/20% CO_2 to adapt them to autotrophic metabolisms.
429 The methanol-adapted *S.ovata* was cultured in the yeast media containing 2% methanol as a
430 sole electron donor before the two hydrogen cycles to upregulate the methanol oxidizing
431 pathways.

432 The hydrogen-grown *S. ovata* cells were inoculated into the prepared anaerobic cathodic
433 chamber with a final OD_{545} of ~0.08. After the inoculation, the applied electrochemical bias
434 was set at ~0.3 V vs. RHE or a potential which gives ~100 $\mu A/cm^2$. and the inoculated cells
435 were cultured for another day. The purging gas was changed to 80% N_2/20% CO_2 (without H_2),
436 and the applied bias was increased at 0.2 V vs. RHE. The SiNW photocathode served as the
437 sole electron donor after this point. After one-day incubation on the photoelectrode, half of the
438 catholyte was exchanged with a fresh anaerobic electrolyte. This procedure was repeated in
439 one day, and the catholyte became clear (<0.04 OD_{545}) as most of bacterial cells were attached
440 on the SiNWs array or removed during exchange. Then, the stable bacteria-nanowire hybrids
441 were ready for a cathodic half-reaction or bias-free operation.

442 **Cathodic product analysis**

Liquid products for CO_2 reduction from the cathode were quantified after electrolysis by proton nuclear magnetic resonance (^{1}H-NMR) spectroscopy (Bruker Avance I) with 3-(Trimethylsilyl)propionic-2,2,3,3-d_4 acid sodium salt (TMSP-d4) as an internal standard for quantification. Acetate was the sole detectable product of the CO_2-reducing metabolism of *S. ovata* owing to its highly selective metabolic pathway. 20 vol.% of a D_2O-TMSP standard was added to all the catholyte solutions. The standard solution was prepared by adding 20 mg TMSP to 25 g of D_2O. $FE_{acetate}$ and the incremental mole of acetic acid is calculated based on the following equation:

$$FE_{acetate} = \frac{96485 \times 8 \times \text{incremental mole of acetic acid}}{\int \text{Idt}} \qquad (3)$$

$$\Delta n_{acetic\ acid} = \alpha \frac{A_{acetate,end}}{A_{TMSP}} \times V_{electrolyte} - \alpha \frac{A_{acetate,start}}{A_{TMSP}} \times (V_{electrolyte} - V_{NMR}) \qquad (4)$$

α represents the conversion factor between acetate concentration and the ratio of the NMR peak area of acetate (1.8 ppm) to the NMR peak area of TMSP (0 ppm). The NMR spectrum of catholyte is shown in Supplementary Fig. S5. The factor is determined by the slope of a six-point calibration curve between 0 to 10 mM. $V_{electrolyte}$ is the volume of electrolyte, typically around 15 ml and VNMR is the sampling volume for NMR measurement, typically 0.7 ml. Before starting the reaction, 0.7 ml of electrolyte was sampled, and the fresh electrolyte was subsequently added back to the electrochemical cell to maintain the total volume of electrolyte.

Anodic product analysis

Liquid products for glycerol oxidation from the anode were quantified after electrolysis by 1H-qNMR spectroscopy (Bruker Avance 600) with water suppression using dimethyl sulfoxide (DMSO) as an internal reference. FE was reported as it is without normalization. A relaxation delay of 42 seconds was used. A standard D_2O-DMSO solution was prepared by adding 400 µl of DMSO to 100 g of D_2O. A 10 vol.% of D_2O-DMSO standard was added to the analyte solutions. The equation (3) and (4) same as cathodic product analysis were used for anodic

product analysis, and the number of electrons used for an electrochemical reaction (e.g., 8 for acetate) was modified depending on the oxidation products.

SEM and EDX characterization.

After the PEC characterizations were complete, the SiNW photoelectrodes were subjected to SEM characterization. For the biophotocathodes, an bacteria fixation was conducted by adding 2.5% glutaraldehyde to the catholyte. After ~18 hours, the glutaraldehyde solution was removed and the PEC cell was washed with DI water two times and the PEC cell was disassembled. The prepared biocathode was followed by dehydration process by gradually increasing ethanol concentrations in water (12.5%, 25%, 37.5%, 50%, 62.5%, 75%, 87.5%, 100%, for 10 minutes each). For the abiotic photocathodes, the electrolyte was replaced with ethanol to prevent the fingering of nanowires due to a high surface tension of water. Prior to electron imaging, the center of Si electrode was cleaved with a diamond scriber and then sputtered with ~3 nm of Au (Denton Vacuum). Benchtop SEM (JEOL, JCM-7000) was used for visualization of the bacteria-nanowire interface, and field emission SEM (Thermo Fisher Scientific, Scios 2 FIB/SEM) was used for SEM/EDX analysis.

XRD and XPS characterization

Powder X-ray diffraction data were collected using a Bruker D8 laboratory diffractometer with a Cu Kα ($\lambda_{K\alpha1}$ = 1.5406 Å, $\lambda_{K\alpha2}$ = 1.54439 Å) radiation source under ambient conditions. Data were collected at 2θ = 20–60° with a step size of 0.0158399° s^{-1}.

XPS (Thermo Scientific K-Alpha) was used for the characterization of elemental states of ALD TiO_2 film. For XPS measurements, monochromatic Al Kα was used with a spot size of 400 μm and pass energy of 50 eV. Three different spots on a sample were chosen to get a representative measurement of the sample.

EIS characterization

EIS was used to measure the solution resistance of 0.5 M sulfuric acid and the bacterial medium. The EIS measurements were conducted at the open circuit potential (OCP) of the cathodes, and the OCP was measured for 1 minute right before the EIS measurements. The measurements were conducted from 1 kHz to 10 Hz with a 10 mV AC voltage and 10 points per decade. The data analysis was performed with the Gamry Echem Analyst software.

Data availability

The data that support the findings of this study are available within the Article and Supplementary Information or from the corresponding author upon reasonable request.

Acknowledgments

We thank the Marvell Nanofabrication Laboratory at UC Berkeley for use of their facilities. We thank Dr. Hasan Celik and UC Berkeley's NMR facility in the College of Chemistry (CoC-NMR) for spectroscopic assistance. This work was supported by the National Science Foundation grant DMR-221716. Jimin. K. acknowledges the fellowship support from Kwanjeong educational foundation. J. -A. L. thanks the financial support from the Taiwan Ministry of Education and Liquid Sunlight Alliance, which is supported by the U.S. Department of Energy, Office of Science, Office of Basic Energy Sciences, Fuels from Sunlight Hub under award DE-SC0021266. Instruments in the CoC-NMR are supported in part by National Institutes of Health grant S10OD024998.

Author contributions

Jimin K. and P. Y. designed the experiments. J.-A. L., and I. R. fabricated the silicon nanowire electrodes. Jimin K., and Jinhyun K. performed the bacteria culturing and incubation. Jimin K., J. -A. L, and Jinhyun K. did the electrochemical and light-driven experiments. Jimin K., J

-A. L., and P. Y. co-wrote the paper. All authors discussed the results and revised the manuscript.

Competing interests

Authors declare that they have no competing interests.

Figure legends

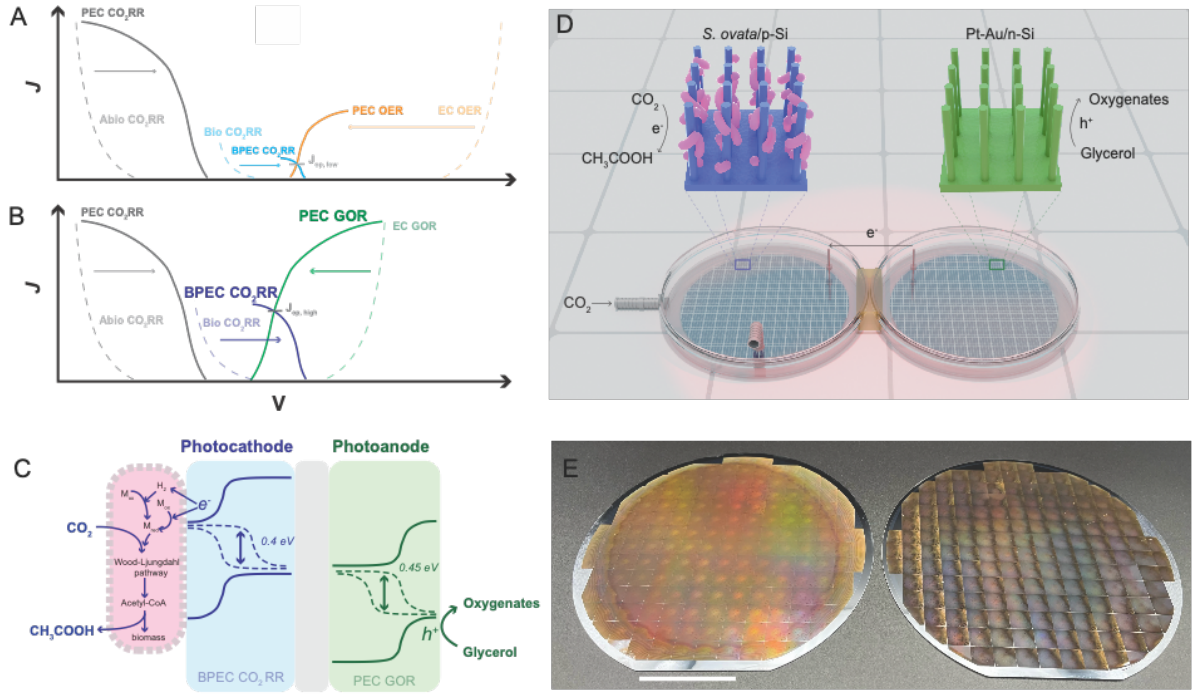

Fig. 1. Overview of SiNW biophotochemical diodes for simultaneous CO_2RR and GOR. (**A, B**) Schematic current density-voltage curves of electrochemical (EC) and PEC conditions for abiotic CO_2RR (grey), biotic CO_2RR (blue), GOR (green), and OER (orange). Predicted operating photocurrent densities of bias-free systems are shown for PEC bioCO_2RR-OER ($J_{op, low}$) and PEC bioCO_2RR-GOR ($J_{op, high}$). (**C**) Schematic energy diagram of a photochemical diode under red light irradiation. A photovoltage of 0.4 V was harvested at the photocathode, and a photovoltage of 0.45 V was harvested at the photoanode, coupling CO_2RR and GOR under red light irradiation without an external bias. **(D)** Schematics of a bias-free photochemical diode device consisting of a photocathode and a photoanode separated by a

bipolar membrane under red light irradiation. A magnified illustration of a p-type SiNW biophotocathode (blue) and an n-type SiNW photoanode (green) shows the reaction interface of the two photoelectrodes. *S. ovata* (pink) was used as a cathodic microbial catalyst for CO_2RR, and co-sputtered Pt-Au was used as an anodic catalyst for GOR. **(E)** A photograph of a wafer-scale nanofabricated 6-inch n^+p-SiNW photocathode (left) and p^+n-SiNW photoanode (right). Scale bar, 5 cm **(E)**

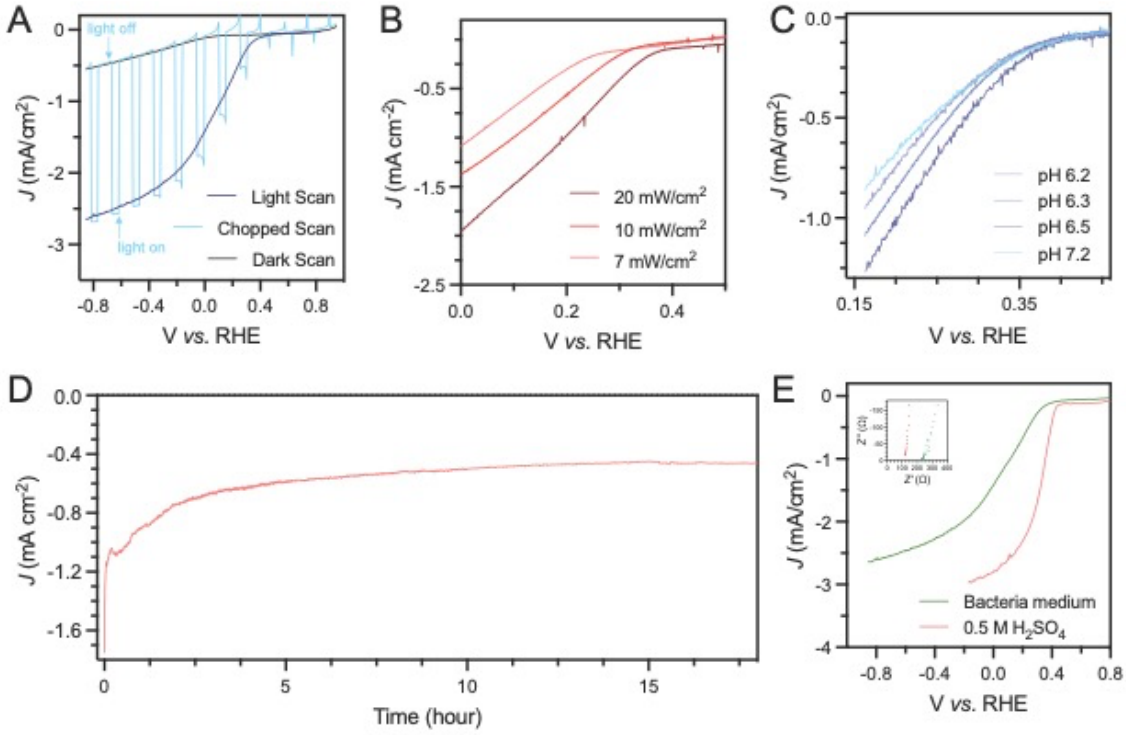

Fig. 2. Photoelectrochemistry of abiotic SiNW photocathodes in neutral pH buffer. (**A)** Photocurrent densities versus bias (vs. RHE) of Pt/TiO_2/n^+p-SiNW photocathodes under 20 mW/cm^2 of 740 nm red light LED irradiation, chopped irradiation (light on/off), and dark condition (**B)** Photocurrent densities versus bias (vs. RHE) of the SiNW photocathodes under the different intensities of red light irradiation. (**C)** Photocurrent densities versus bias (vs. RHE) of SiNW photocathodes under the different pH of electrolytes. (**D)** Current density traces versus time for the SiNW photocathodes using the bacterial medium with pH 6.2 at the applied potential of 0.15 V vs. RHE. (**E)** Photocurrent densities versus applied bias (vs. RHE) using 0.5 M sulfuric acid (red) and the bacterial medium (green) with the SiNW photocathodes under red light irradiation. The scan rate of all LSV measurements was 10 mV/sec. The catholyte was continuously purged with an 80% N_2/20% CO_2 gas.

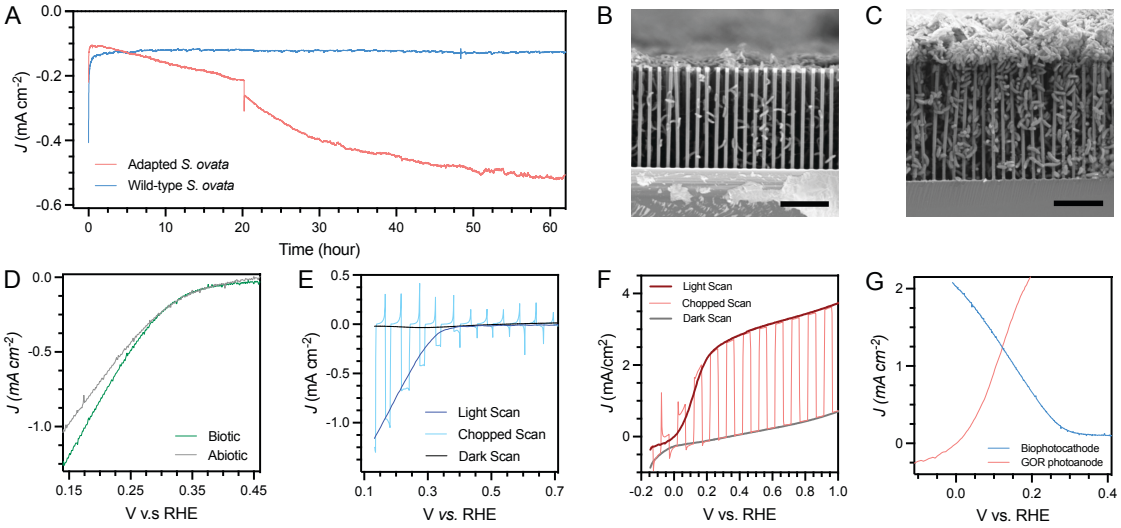

549

550 **Fig. 3. SiNW biophotocathodes for CO_2RR and SiNW photoanodes for GOR.** **(A)** Time
551 evolution of photocurrent densities of SiNW biophotocathodes using wild-type *S. ovata* (blue)
552 and methanol-adapted *S. ovata* (red) at ~0.2 V vs. RHE. Cross-sectional SEM images of the
553 biophotocathodes integrated with **(B)** wild-type *S. ovata* and **(C)** methanol-adapted *S. ovata*
554 after ~62 hours of PEC operations. The SEM images shown in B and C are representative of at
555 least three independent experiments. The scale bars are 10 μ m. **(D)** Representative
556 photocurrent densities versus bias (vs. RHE) of SiNW photocathodes with (Biotic, green) and
557 without (Abiotic, grey) adapted *S. ovata*. **(E)** Photocurrent densities versus bias (vs. RHE) of
558 SiNW biophotocathodes with adapted *S. ovata* under continuous irradiation, chopped
559 irradiation, and dark conditions**. (F)** Photocurrent densities versus bias (vs. RHE) of GOR using
560 Pt-Au/TiO_2/p^+n-SiNW photoanode in 1M KOH + 0.1M glycerol under continuous irradiation,
561 chopped irradiation, and dark. **(G)** The overlap of *J-V* scans of the biophotocathode and the
562 photoanode on an RHE scale. The current density of the biophotocathode was converted from
563 negative to positive. A 20 mW/cm^2 of red light (740 nm) was used as a light source. The scan
564 rate of all LSV measurements was 10 mV/sec. The catholyte was continuously purged with an
565 80% N_2/20% CO_2 gas.

566

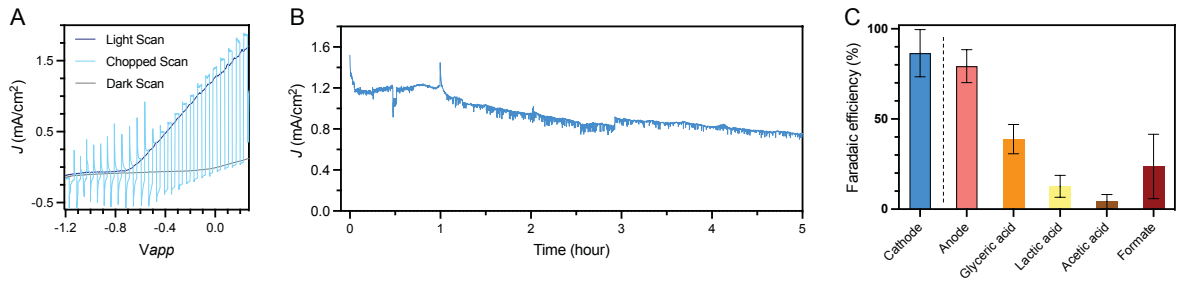

567

568 **Fig. 4. PEC performance of the biophotochemical diodes in a two-electrode**
569 **configuration.** (**A)** Photocurrent densities versus applied bias (vs. RHE) of the
570 biophotochemical diodes combining *S.ovata*/Pt/TiO_2/n^+p-SiNW and Pt-Au/TiO_2/p^+n-SiNW
571 photoanode under continuous irradiation, chopped irradiation, and dark**.** An applied voltage
572 of 0 V between two electrodes indicates the bias-free condition. (**B)** Photocurrent density
573 traces of the bias-free biophotochemical diodes under continuous red light irradiation. (**C)**
574 Faradaic efficiencies of the cathodic product (blue) and the total anodic products (pink) and
575 each anodic product under the bias-free operation of the biophotochemical diodes. A 20
576 mW/cm^2 of red light (740 nm) was used as a light source. The scan rate of all LSV
577 measurements was 10 mV/sec. The bacterial medium, pH 6.2, was used as the catholyte,
578 and 0.1M glycerol in 1M KOH was used as the anolyte. The catholyte was continuously
579 purged with an 80% N_2/20% CO_2 gas. Error bars represent the standard deviation from three
580 independent measurements.

581

582

583 **References**

584 1. Chu, S., Cui, Y. & Liu, N. The path towards sustainable energy. *Nat. Mater.* **16**, 16–22
585 (2016).

586 2. Yin, J., Molini, A. & Porporato, A. Impacts of solar intermittency on future photovoltaic
587 reliability. *Nat. Commun.* **11**, 1–9 (2020).

588 3. Kim, D., Sakimoto, K. K., Hong, D. & Yang, P. Artificial photosynthesis for sustainable
589 fuel and chemical production. *Angew. Chemie - Int. Ed.* **54**, 3259–3266 (2015).

590 4. Deng, J. *et al.* Nanowire Photoelectrochemistry. *Chem. Rev.* **119**, 9221–9259 (2019).

591 5. Kim, J. *et al.* Robust FeOOH/BiVO4/Cu(In, Ga)Se2tandem structure for solar-powered
592 biocatalytic CO2reduction. *J. Mater. Chem. A* **8**, 8496–8502 (2020).

593 6. Kuk, S. K. *et al.* CO2-Reductive, Copper Oxide-Based Photobiocathode for Z-Scheme
594 Semi-Artificial Leaf Structure. *ChemSusChem* **13**, 2940–2944 (2020).

595 7. Nozik, A. J. Photochemical diodes. *Appl. Phys. Lett.* **30**, 567–569 (1977).

596 8. Andrei, V., Roh, I. & Yang, P. Nanowire photochemical diodes for artificial
597 photosynthesis. *Sci. Adv.* **9**, 1–21 (2023).

598 9. Sivula, K. & Van De Krol, R. Semiconducting materials for photoelectrochemical
599 energy conversion. *Nat. Rev. Mater.* **1**, (2016).

600 10. Liu, C., Tang, J., Chen, H. M., Liu, B. & Yang, P. A fully integrated nanosystem of
601 semiconductor nanowires for direct solar water splitting. *Nano Lett.* **13**, 2989–2992
602 (2013).

603 11. Sokol, K. P. *et al.* Bias-free photoelectrochemical water splitting with photosystem II
604 on a dye-sensitized photoanode wired to hydrogenase. *Nat. Energy* **3**, 944–951 (2018).

605 12. Ryu, H. K. S. B. D. J. J. Fully solution-processable Cu2O–BiVO4 photoelectrochemical

606 cells for bias-free solar water splitting. *Green Chem.* **20**, 3732–3742 (2018).

607 13. Li, C. *et al.* Photoelectrochemical CO2 reduction to adjustable syngas on grain-
608 boundary-mediated a-Si/TiO2/Au photocathodes with low onset potentials. *Energy*
609 *Environ. Sci.* **12**, 923–928 (2019).

610 14. Gurudayal *et al.* Si photocathode with Ag-supported dendritic Cu catalyst for CO2
611 reduction. *Energy Environ. Sci.* **12**, 1068–1077 (2019).

612 15. Rahaman, M. *et al.* Solar-driven liquid multi-carbon fuel production using a standalone
613 perovskite–BiVO4 artificial leaf. *Nat. Energy* **8**, 629–638 (2023).

614 16. Nevin, K. P., Woodard, T. L., Franks, A. E., Summers, Z. M. & Lovley, D. R. Microbial
615 Electrosynthesis: Feeding Microbes Electricity To Convert Carbon Dioxide and Water
616 to Multicarbon Extracellular Organic Compounds Kelly. *MBio 1* **1**, e00103–e00110.
617 (2010).

618 17. Liu, C. *et al.* Nanowire-bacteria hybrids for unassisted solar carbon dioxide fixation to
619 value-added chemicals. *Nano Lett.* **15**, 3634–3639 (2015).

620 18. Cestellos-Blanco, S. *et al.* Production of PHB From CO2-Derived Acetate With
621 Minimal Processing Assessed for Space Biomanufacturing. *Front. Microbiol.* **12**, 1–12
622 (2021).

623 19. Cestellos-Blanc, S. *et al.* Photosynthetic biohybrid coculture for tandem and tunable
624 CO2and N2 fixation. *Proc. Natl. Acad. Sci. U. S. A.* **119**, 1–10 (2022).

625 20. Verma, S., Lu, S. & Kenis, P. J. A. Co-electrolysis of CO2 and glycerol as a pathway to
626 carbon chemicals with improved technoeconomics due to low electricity consumption.
627 *Nat. Energy* **4**, 466–474 (2019).

628 21. Lin, J. A., Roh, I. & Yang, P. Photochemical Diodes for Simultaneous Bias-Free

629 Glycerol Valorization and Hydrogen Evolution. *J. Am. Chem. Soc.* (2023).
630 doi:10.1021/jacs.3c01982

631 22. Kim, J., Cestellos-Blanco, S., Shen, Y., Cai, R. & Yang, P. Enhancing Biohybrid CO 2
632 to Multicarbon Reduction via Adapted Whole-Cell Catalysts . *Nano Lett.* (2022).
633 doi:10.1021/acs.nanolett.2c01576

634 23. Yang, F., Hanna, M. A. & Sun, R. Value-added uses for crude glycerol–a byproduct of
635 biodiesel production. *Biotechnol. Biofuels* **5**, 1–10 (2012).

636 24. Schuchmann, K. & Müller, V. Autotrophy at the thermodynamic limit of life: A model
637 for energy conservation in acetogenic bacteria. *Nat. Rev. Microbiol.* **12**, 809–821 (2014).

638 25. Lewis, N. S. & Nocera, D. G. Powering the planet: Chemical challenges in solar energy
639 utilization. *Proc. Natl. Acad. Sci. U. S. A.* **103**, 15729–15735 (2006).

640 26. Brito-Santos, G. *et al.* Degradation analysis of highly UV-resistant down-shifting layers
641 for silicon-based PV module applications. *Mater. Sci. Eng. B Solid-State Mater. Adv.*
642 *Technol.* **288**, (2023).

643 27. Wang, Y. *et al.* Antimicrobial Blue Light Inactivation of Gram-Negative Pathogens in
644 Biofilms: In Vitro and in Vivo Studies. *J. Infect. Dis.* **213**, 1380–1387 (2016).

645 28. Lipovsky, A., Nitzan, Y., Gedanken, A. & Lubart, R. Visible light-induced killing of
646 bacteria as a function of wavelength: Implication for wound healing. *Lasers Surg. Med.*
647 **42**, 467–472 (2010).

648 29. Su, Y. *et al.* Single-nanowire photoelectrochemistry. *Nat. Nanotechnol.* **11**, 609–612
649 (2016).

650 30. Liu, C. *et al.* Nanowire−Bacteria Hybrids for Unassisted Solar Carbon Dioxide Fixation.
651 *Nano Lett.* **15**, 3634–3639 (2015).

652 31. Boettcher, S. W. *et al.* Photoelectrochemical hydrogen evolution using Si microwire
653 arrays. *J. Am. Chem. Soc.* **133**, 1216–1219 (2011).

654 32. Lineberry, E. *et al.* High-Photovoltage Silicon Nanowire for Biological Cofactor
655 Production. (2023). doi:10.1021/jacs.3c06243

656 33. Gebresemati, M., Das, G., Park, B. J. & Yoon, H. H. Electricity production from
657 macroalgae by a microbial fuel cell using nickel nanoparticles as cathode catalysts. *Int.*
658 *J. Hydrogen Energy* **42**, 29874–29880 (2017).

659 34. Hernández, L. A., Riveros, G., González, D. M., Gacitua, M. & del Valle, M. A.
660 PEDOT/graphene/nickel-nanoparticles composites as electrodes for microbial fuel cells.
661 *J. Mater. Sci. Mater. Electron.* **30**, 12001–12011 (2019).

662 35. Can, M., Armstrong, F. A. & Ragsdale, S. W. Structure, function, and mechanism of the
663 nickel metalloenzymes, CO dehydrogenase, and acetyl-CoA synthase. *Chem. Rev.* **114**,
664 4149–4174 (2014).

665 36. Barolet, D., Christiaens, F. & Hamblin, M. R. Infrared and skin: Friend or foe. *J.*
666 *Photochem. Photobiol. B Biol.* **155**, 78–85 (2016).

667 37. Su, Y. *et al.* Close-Packed Nanowire-Bacteria Hybrids for Efficient Solar-Driven CO2
668 Fixation. *Joule* **4**, 800–811 (2020).

669 38. Moore, E. E. *et al.* Understanding the local chemical environment of bioelectrocatalysis.
670 *Proc. Natl. Acad. Sci. U. S. A.* **119**, (2022).

671 39. Möller, B., Oßmer, R., Howard, B. H., Gottschalk, G. & Hippe, H. Sporomusa, a new
672 genus of gram-negative anaerobic bacteria including Sporomusa sphaeroides spec. nov.
673 and Sporomusa ovata spec. nov. *Arch. Microbiol.* **139**, 388–396 (1984).

674 40. Salimijazi, F., Kim, J., Schmitz, A., Grenville, R. & Barstow, B. Constraints on the

675 Efficiency of Electromicrobial Production 1. *Joule* (2020).
676 doi:10.1101/2020.06.23.167288

677 41. Jourdin, L. & Burdyny, T. Microbial Electrosynthesis: Where Do We Go from Here?
678 *Trends Biotechnol.* **39**, 359–369 (2021).

679 42. Prévoteau, A., Carvajal-Arroyo, J. M., Ganigué, R. & Rabaey, K. Microbial
680 electrosynthesis from CO2: forever a promise? *Curr. Opin. Biotechnol.* **62**, 48–57
681 (2020).

682 43. Tremblay, P. L., Höglund, D., Koza, A., Bonde, I. & Zhang, T. Adaptation of the
683 autotrophic acetogen Sporomusa ovata to methanol accelerates the conversion of CO2
684 to organic products. *Sci. Rep.* **5**, 1–11 (2015).

685 44. Mccuskey, S. R., Su, Y., Leifert, D., Moreland, A. S. & Bazan, G. C. Living
686 Bioelectrochemical Composites. *Adv. Mater.* **1908178**, 1–6 (2020).

687 45. Qian, J. *et al.* Barcoded microbial system for high-resolution object provenance. *Science*
688 *(80-.).* **1140**, 1135–1140 (2020).

689 46. Luo, L. *et al.* Selective Photoelectrocatalytic Glycerol Oxidation to Dihydroxyacetone
690 via Enhanced Middle Hydroxyl Adsorption over a Bi2O3-Incorporated Catalyst. *J. Am.*
691 *Chem. Soc.* **144**, 7720–7730 (2022).

692 47. Li, J. *et al.* Tuning the Product Selectivity toward the High Yield of Glyceric Acid in
693 Pt−CeO2/CNT Electrocatalyzed Oxidation of Glycerol. *ChemCatChem* **14**, e202200509
694 (2022).

695 48. Luo, J. *et al.* Bipolar Membrane-Assisted Solar Water Splitting in Optimal pH. *Adv.*
696 *Energy Mater.* **6**, 1–7 (2016).

697 49. Kong, Q. *et al.* Directed Assembly of Nanoparticle Catalysts on Nanowire

Photoelectrodes for Photoelectrochemical CO2 Reduction. *Nano Lett.* **16**, 5675–5680 (2016).

50. Seger, B. *et al.* Using TiO2 as a conductive protective layer for photocathodic H2 evolution. *J. Am. Chem. Soc.* **135**, 1057–1064 (2013).

51. Yu, Y. *et al.* Enhanced photoelectrochemical efficiency and stability using a conformal TiO2 film on a black silicon photoanode. *Nat. Energy* **2**, (2017).